de Haas–van Alphen quantum oscillations and electronic structure in the large-Chern-number topological chiral semimetal CoSi

Huan Wang,[*] Sheng Xu [®],[*] Xiao-Qin Lu,[*] Xiao-Yan Wang, Xiang-Yu Zeng, Jun-Fa Lin, Kai Liu, Zhong-Yi Lu, and Tian-Long Xia[†]

Department of Physics, Renmin University of China, Beijing 100872, People's Republic of China
and Beijing Key Laboratory of Opto-electronic Functional Materials & Micro-nano Devices, Renmin University of China, Beijing 100872,
People's Republic of China

We investigate the magnetic transport properties and electronic structures of single crystal CoSi via angle-dependent quantum oscillation measurements. Prominent de Haas–van Alphen oscillations have been observed with the magnetic field tilting from $B \parallel [001]$ to $B \parallel [110]$, from which three fundamental frequencies are extracted. The low frequency F_α, first observed in quantum oscillations, presents the contribution from the hole pocket at the Brillouin zone (BZ) center Γ point. Two high frequencies F_β and F_γ, accompanied with asymmetrical peaks in the fast Fourier-transform spectra, are confirmed to stem from the electron pockets with spin-orbit coupling (SOC) at the BZ corner R point. Combined with the analysis of first-principles calculations, the asymmetry of peaks originate from the SOC-induced band splitting when $B \parallel [110]$ and the irregular Fermi pockets when $B \parallel [001]$, respectively.

I. INTRODUCTION

The exploration and study on fermions lay a foundation for realizing exotic physical phenomena. Dirac and Weyl semimetals which host the massless Dirac or Weyl fermions have attracted tremendous attention due to their novel properties, such as high mobility, low carrier concentration, large magnetoresistance (MR), chiral-anomaly-induced negative MR, and so on [1–25]. Besides the well known spin-1/2 Weyl fermion [14–25], some new types of fermionic excitations which include spin-1 excitation, spin-3/2 Rarita-Schwinger-Weyl (RSW) fermion, and double Weyl fermion have been found in condensed matter physics [26–34]. Recently, CoSi and its family materials are confirmed to hold these new types of fermionic excitations [28,32,34–46].

CoSi holds the spin-1 excitation with Chern number $+2$ at R and the double Weyl fermion with the Chern number -2 at R. The spin-orbit coupling (SOC) lifts the degeneracy of the energy band, which makes the spin-1 excitation evolve into the spin-3/2 RSW fermion carrying large Chern number $+4$ and the double Weyl fermion evolve into the time-reversal (TR) doubling of spin-1 excitation carrying total large Chern number -4, respectively. These new types of fermions with large Chern number in CoSi are verified in recent experiments, such as angle-resolved photoemission spectroscopy (ARPES) experiments [36–38], thermoelectric quantum oscillations [39], and Shubnikov–de Haas (SdH) quantum oscillations [40].

We study the electronic structures of CoSi via de Haas–van Alphen (dHvA) oscillations and the first-principles calculations. Evident angle-dependent dHvA quantum oscillations with magnetic field rotating from $B \parallel [001]$ to $B \parallel [110]$ have been observed, from which three main frequencies are extracted. The low frequency F_α, absent in previous quantum oscillations [39,40], is observed and verified to stem from the hole pocket at Γ. Two high frequencies F_β and F_γ, consistent with previous reports [36–40], are confirmed to originate from the electron pockets with SOC at R. In addition, the asymmetry exists in the peaks of F_β and F_γ in the fast Fourier-transform (FFT) spectra. Combined with the analysis of the first-principles calculations, the asymmetry of peaks stem from the SOC-induced band splitting when $B \parallel [110]$ and the irregular Fermi pockets when $B \parallel [001]$, respectively. The light effective masses are extracted from the fitting of the thermal damping term in the Lifshitz-Kosevich (LK) formula, indicating the possible existence of a new type of massless fermions.

II. EXPERIMENTAL AND CRYSTAL STRUCTURE

The high quality single crystals of CoSi were grown by flux method [39]. The mixture of Co powder, Si powder, and Te lump with the ratio of 1:1:20 was loaded into a corundum crucible which was sealed into a quartz tube. Then the tube was put into a furnace and heated to $1150\,°C$ for 20 h to allow sufficient homogenization, then cooled down to $700\,°C$ at a rate of $3\,°C/h$. Finally, crystals with metallic luster were obtained by centrifugation to remove excess flux at $700\,°C$. The atomic composition was confirmed to be Co:Si $= 1:1$ by energy dispersive x-ray spectroscopy (EDS, Oxford X-Max 50). The single-crystal x-ray diffraction (XRD) pattern and

---

[*]These authors contributed equally to this paper.
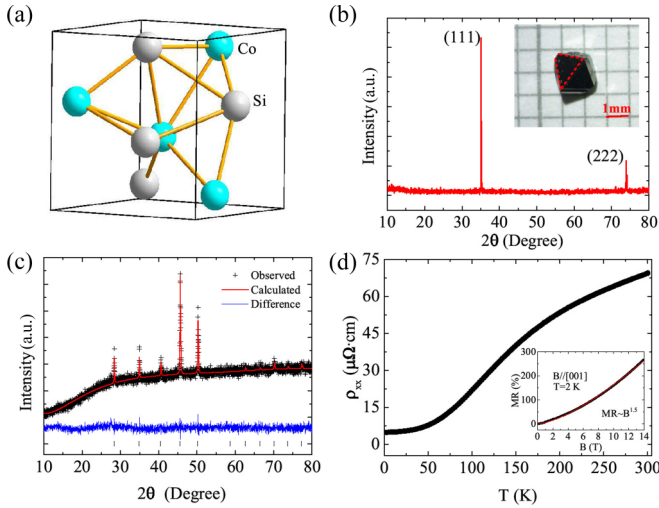[†]tlxia@ruc.edu.cn

115129-1

FIG. 1. (a) Crystal structure of CoSi with the space group $P2_13$ (No. 198). (b) Single crystal XRD pattern of CoSi. Inset shows the picture of grown single crystal. (c) Powder XRD pattern with refinement. (d) The temperature-dependent resistivity from 2 K to 300 K with the RRR ≈ 14. Inset shows the MR versus magnetic field at 2 K with $B \parallel [001]$ configuration.

FIG. 2. (a) Magnetization versus magnetic field at various temperatures. (b) The amplitudes of dHvA oscillations as a function of $1/B$. (c) The FFT spectra of the oscillations. Inset shows the temperature dependence of relative FFT amplitude of the frequencies.

powder XRD patterns were carried out by a Brucker D8 Advance X-ray diffractometer using Cu K_α radiation. TOPAS-4.2 was employed for the refinement. The measurements of resistivity and magnetic properties were performed on a Quantum Design physical property measurement system (QD PPMS-14 T). The first-principles electronic structure calculations of CoSi were performed by using the projector augmented wave (PAW) method [47,48], as implemented in the VASP package [49–51]. The generalized gradient approximation (GGA) of Perdew-Burke-Ernzerhof (PBE) type [52] was used for the exchange-correlation functional. The kinetic energy cutoff of the plane-wave basis was set to be 400 eV. The Brillouin zone (BZ) was sampled with a $16 \times 16 \times 16$ k-point mesh. For the Fermi surface (FS) broadening, the Gaussian smearing method with a width of 0.01 eV was adopted. Both lattice parameters and internal atomic positions were fully relaxed until all the forces on atoms were smaller than 0.01 eV/Å. The calculated lattice constants of CoSi (4.427 Å) agree well with the experimental values of 4.45 Å [53]. The SOC effect was included in the band structure calculations. The FSs were studied by the maximally localized Wannier functions (MLWF) method [54,55].

The crystal structure of CoSi with space group $P2_13$ (No. 198) is shown in Fig. 1(a). The single-crystal XRD pattern illustrated in Fig. 1(b) reveals the (111) crystalline surface. The inset of Fig. 1(b) displays a photography of a CoSi single crystal with metallic luster. Figure 1(c) shows the powder XRD patterns (a powdered sample was obtained by crushing single crystals) which can be well refined with space group $P2_13$, and the refined lattice parameter is $a = b = c = 4.446$ Å. The hump at small angle (below $27°$) may be induced by the adsorption of water into the sample, which is hard to remove even when the Kapton film is employed. As displayed in Fig. 1(d), the temperature-dependent resistivity ρ_{xx} demonstrates the metallic behavior with the residual resistance ratio (RRR ≈ 14).
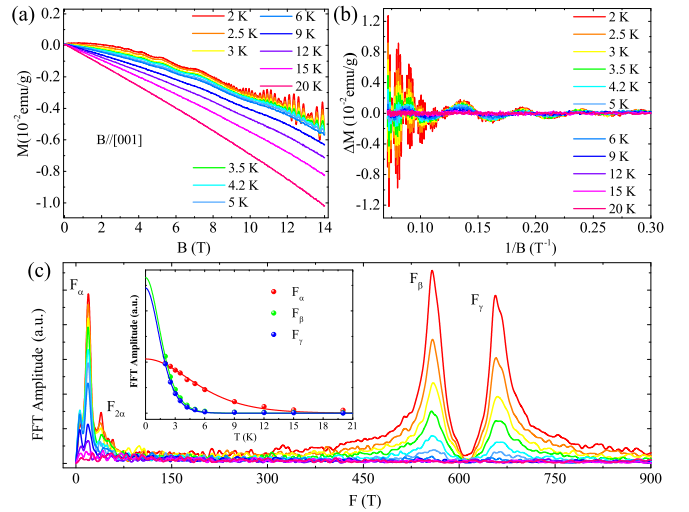
III. RESULTS AND DISCUSSION

Quantum oscillation experiments provide an effective method to study the electronic structures of a single crystal. Evident dHvA quantum oscillations have been observed in CoSi at low temperature and high magnetic field with $B \parallel [00l]$ configuration, as shown in Fig. 2(a). The periodic oscillations $\Delta M = M - \langle M \rangle$ are obtained after subtracting a smooth background, which is plotted as a function of $1/B$ in Fig. 2(b). Three prominent frequencies are extracted from the FFT analysis, which are indexed as $F_\alpha = 19.7$ T, $F_\beta = 557.6$ T, and $F_\gamma = 656.7$ T, as shown in Fig. 2(c). The extreme cross section A_F of FS normal to the magnetic field can be obtained according to the Onsager relation $F = (\hbar/2\pi e)A_F$. Thus the corresponding results are $A_F^\alpha \approx 1.87 \times 10^{-3}$ Å^{-2}, $A_F^\beta \approx 53.21 \times 10^{-3}$ Å^{-2}, and $A_F^\gamma \approx 62.66 \times 10^{-3}$ Å^{-2}, respectively. Among them, the frequency F_α is first detected in quantum oscillation measurements. Two high frequencies F_β and F_γ are consistent with previous reports [36–40]. In addition, the asymmetry of peaks F_β and F_γ in FFT spectra are detected [Fig. 2(c)], which indicates the composition of two close frequencies.

The oscillatory component can be described by the LK formula [56]:

$$\Delta M \propto -B^{1/2} \frac{\lambda T}{\sinh(\lambda T)} e^{-\lambda T_D} \sin\left[2\pi\left(\frac{F}{B} - \frac{1}{2} + \beta + \delta\right)\right],$$ (1)

where $\lambda = (2\pi^2 k_B m^*)/(\hbar e B)$ and T_D is the Dingle temperature. $\beta = \Phi_B/2\pi$ and Φ_B is the Berry phase. The phase shift δ is determined by the dimensionality $\delta = 0$ and $\delta = \pm 1/8$ for 2D and 3D systems, respectively. The thermal damping factor $R_T = (\lambda T)/\sinh(\lambda T)$ in the LK formula is employed to fit the temperature dependence of the FFT amplitude [inset of Fig. 2(c)], from which the light effective masses are obtained and listed in Table I. Angle-dependent dHvA quantum oscillation measurements are further applied to investigate the detailed characteristics of FS. The schematic diagram with the

TABLE I. Parameters extracted from dHvA oscillations in CoSi. F is the frequency of dHvA oscillations; m^*/m_e is the ratio of the effective mass to the electron mass; A_F represents the extreme cross section of the FS and k_F is the Fermi wave vector.

	$F(T)$	m^*/m_e	A_F ($\times 10^{-3}$ Å^{-2})	k_F ($\times 10^{-2}$ Å^{-1})
F_α	19.6	0.11	1.87	2.44
F_β	557.6	0.36	53.21	13.04
F_γ	656.7	0.37	62.66	14.12

magnetic field rotating from $B \parallel [001]$ to $B \parallel [110]$ is drawn in Fig. 3(a). The amplitudes of oscillations versus $1/B$ with the magnetic field along different orientations are shown in Fig. 3(b). The corresponding extracted FFT spectra at typical angle is illustrated in Fig. 3(c). Three fundamental frequencies are observed with different magnetic field orientations. The asymmetry of peaks F_β and F_γ in FFT spectra are also detected, as demonstrated in Fig. 3(c), indicating the existence of two close frequencies. In order to distinguish the frequencies, the multiple peak fits of F_β and F_γ are conducted, the details of which are displayed in the Supplemental Material [57]. To further investigate the origin of this phenomena, the first-principles electronic structure calculations and the detailed analysis are employed.

Figure 4(a) exhibits the band structures of CoSi with SOC included. Figures 4(b) and 4(c) illustrate the enlarged band structures around Γ and R, respectively. The band crossing at R locates at 192 meV below the Fermi level. To aid clarity, the overall three-dimensional (3D) FSs in the first BZ are shown in Fig. 5(a). There are two electron pockets at R along R-X [Fig. 4(c)], indexed as electron pocket 1 (EP1) shown in Fig. 6(a) for (001) plane projection and Fig. 6(b) for (110) plane projection and electron pocket 2 (EP2) shown in Fig. 6(c) for (001) plane projection and Fig. 6(d) for (110) plane projection. They are calabash-shaped instead of perfectly spherical, which contributes to four extreme cross

FIG. 4. (a) Band structure of CoSi calculated with SOC effect. The enlarged band structures around (b) Γ point and (c) R point, respectively.

sections when $B \parallel [001]$. The FS cut in the $k_z = \pi$ plane is displayed in Fig. 5(b). Two extreme cross sections of FSs at R stem from two splitting bands indexed as OE and OF along R-X [Fig. 4(c)], respectively. According to the Onsager relation, the extreme cross sections correspond to frequencies in experiment. Thus, when $B \parallel [001]$, two main frequencies
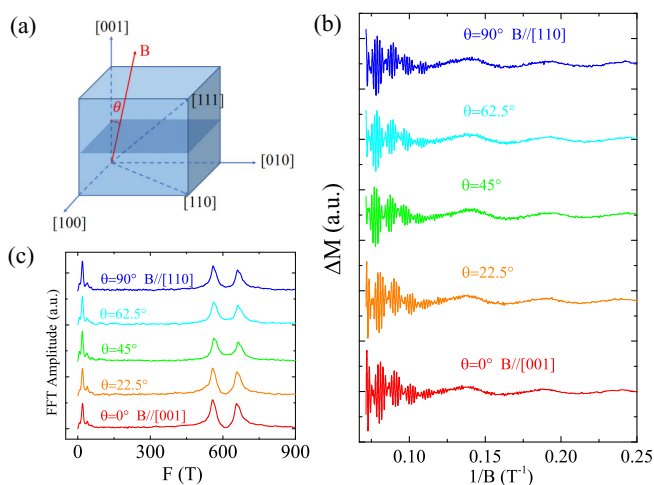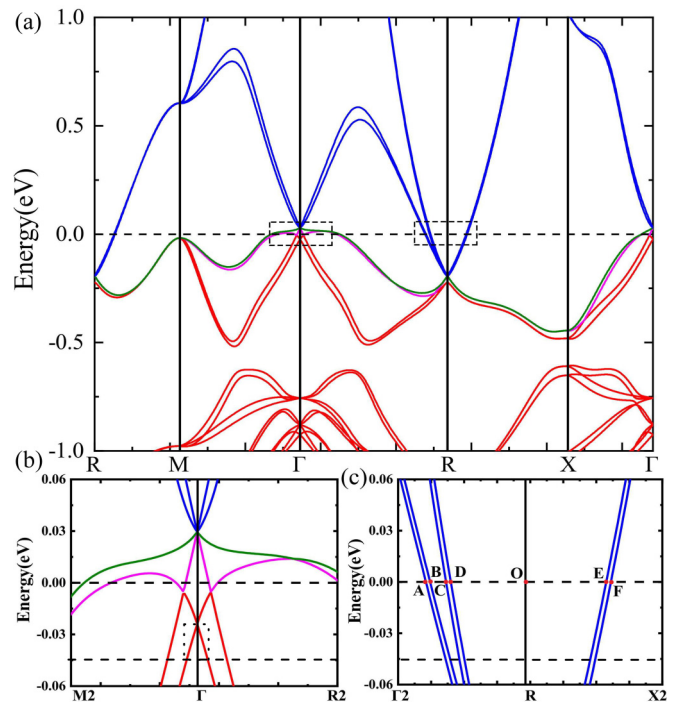

FIG. 3. (a) Diagram of magnetic field B rotating direction along crystallographic direction. (b) The amplitudes of dHvA oscillations versus $1/B$ at different angles. (c) The FFT spectra of the oscillations at different angles.
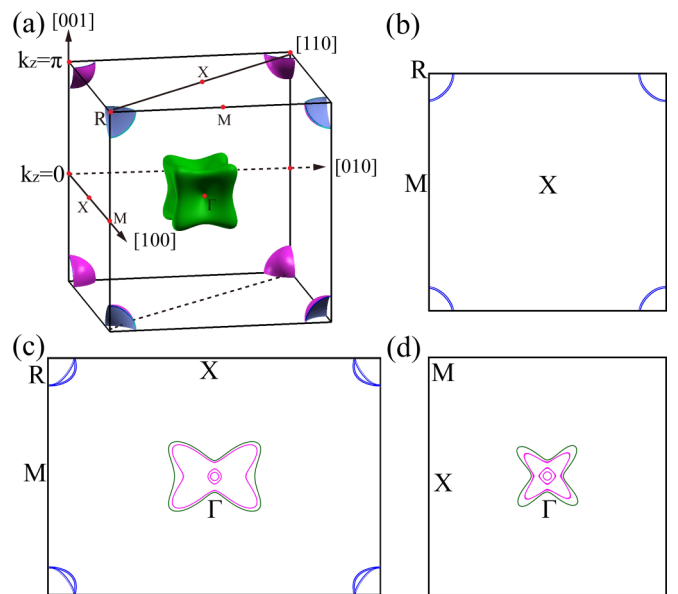

FIG. 5. (a) Calculated electron and hole FS sheets in the bulk BZ of CoSi. Calculated FSs in (b) $k_z = \pi$ plane, (c) (110) plane, and (d) $k_z = 0$ plane, respectively. The colors of 2D FSs have one-to-one correspondence to the colors of bands in Fig. 4.
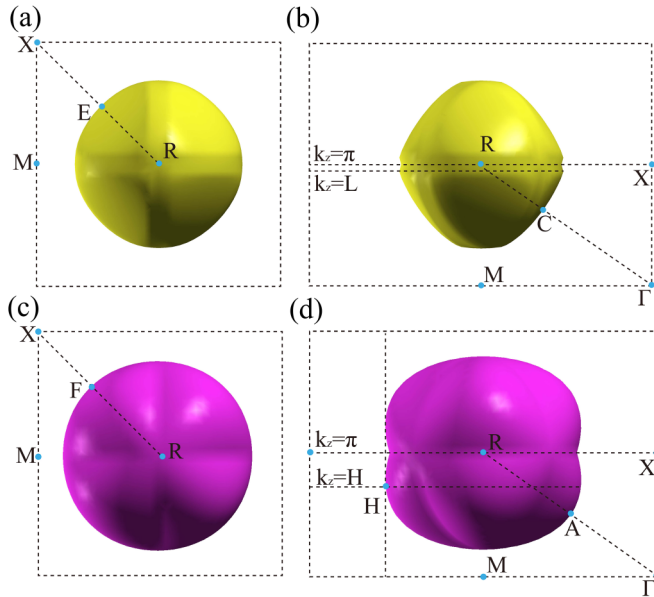
FIG. 6. Top view and side view of the enlarged FSs projected in the (a),(c) (001) plane and (b),(d) (110) plane of BZ, respectively. The letters on the FSs correspond to the letters on bands in Fig. 4(c).

F_β and F_γ originate from the extreme cross sections of EP1 and EP2 at R along the $k_z = \pi$ plane. Figures 6(a) and 6(c) display the detailed profiles of two electron pockets, which also illustrate the identified extremal areas, corresponding to the band OE and OF [Fig. 4(c)], respectively. On the other hand, the asymmetrical peaks F_δ and F_λ (defined in the Supplemental Material [57]) are induced by irregular electron pockets, which stem from the extreme cross sections of EP1 in the $k_z = L$ ($k_z = 0.9396\pi$) and EP2 in the $k_z = H$ ($k_z = 0.9798\pi$) plane, respectively, as displayed in Figs. 6(b) and 6(d). Moreover, the observation of two main frequencies when $B \parallel [001]$ reveals the SOC effect. When the SOC is neglected, only one main asymmetrical frequency, instead of two distinct asymmetrical frequencies, can be observed. The main frequency originates from the extreme cross section in the $k_z = \pi$ plane at R, corresponding to the degenerate band along $R\text{-}X$. The asymmetry of frequency peak originates from the extreme cross section of the irregular electron pocket. The FS cut in the (110) plane is displayed in Fig. 5(c). Four extreme cross sections of FSs at R stem from four splitting bands along R-Γ [Fig. 4(c)], respectively. Therefore, it is natural to detect four frequencies when $B \parallel [110]$. Two fundamental frequencies F_β and F_γ correspond to the bands OD and OB, as shown in Fig. 4(c), respectively (the detailed profiles of electron pockets are displayed in the Supplemental Material [57]). The band splitting induced by SOC leads to the phenomena of obvious asymmetrical peaks observed with $B \parallel [110]$. F_δ and F_λ correspond to the splitting bands OC and OA [Fig. 4(c)], respectively, details of which are illustrated

in Figs. 6(b) and 6(d). In addition, the low frequency F_α, first observed in our dHvA quantum oscillation, is considered to originate from the hole pocket at Γ. However, the mismatch is found when the frequencies obtained from experiment and theory are compared. The measured frequencies are smaller than the theoretical ones. Taking account of the growth method by Te flux, the doping may be brought in and the Fermi level may be shifted, which is also considered in a previous report with the similar growth method [39]. When $B \parallel [001]$, the measured frequencies ($F_\beta = 557.6$ T, $F_\delta = 566.3$ T, $F_\gamma = 656.5$ T, and $F_\lambda = 666.4$ T) are consistent with the calculation ($F'_\beta = 564.3$ T, $F'_\delta = 572.7$ T, $F'_\gamma = 638.2$ T, and $F'_\lambda = 646.7$ T) as the Fermi level is shifted down by 45 meV. Accordingly, the theoretical frequency F_α is 23.4 T with the Fermi level shifted down by 45 meV [the pocket is marked in Fig. 4(b)], which matches very well with the measured frequency (19.7 T). Thus the frequencies F_α, F_β, F_γ, F_δ, and F_λ observed in dHvA oscillations are verified to originate from the Fermi pockets at Γ and R, respectively. Meanwhile, the two distinct frequencies when $B \parallel [001]$ and the asymmetrical peaks observed when $B \parallel [110]$ both affirm the existence of SOC-induced band splitting in CoSi.

IV. SUMMARY

In conclusion, we investigate the magnetic transport properties and electronic structures of CoSi. Evident angle-dependent dHvA quantum oscillations with magnetic field rotating from $B \parallel [001]$ to $B \parallel [110]$ have been observed, from which three fundamental frequencies are extracted. The low frequency F_α is first detected in quantum oscillation measurements, which presents the contribution from the hole pocket at Γ. Two high frequencies F_β and F_γ with asymmetrical peaks are confirmed to originate from the electron pockets at R. Combined with the analysis of first-principles calculations, the asymmetry of peaks are induced by the band splitting due to SOC when $B \parallel [110]$ and the irregular Fermi pockets when $B \parallel [001]$. Thus this paper reveals the hole pocket at Γ and the irregular electron pockets at R, demonstrating the detailed FS characteristics of CoSi with SOC.

[1] Z. Wang, Y. Sun, X.-Q. Chen, C. Franchini, G. Xu, H. Weng, X. Dai, and Z. Fang, Phys. Rev. B **85**, 195320 (2012).

[2] Z. Liu, B. Zhou, Y. Zhang, Z. Wang, H. Weng, D. Prabhakaran, S.-K. Mo, Z. Shen, Z. Fang, X. Dai *et al.*, Science **343**, 864 (2014).

[3] J. Xiong, S. K. Kushwaha, T. Liang, J. W. Krizan, M. Hirschberger, W. Wang, R. Cava, and N. Ong, Science **350**, 413 (2015).

[4] J. Xiong, S. Kushwaha, J. Krizan, T. Liang, R. Cava, and N. Ong, EPL **114**, 27002 (2016).

[5] M. Neupane, S.-Y. Xu, R. Sankar, N. Alidoust, G. Bian, C. Liu, I. Belopolski, T.-R. Chang, H.-T. Jeng, H. Lin *et al.*, Nat. Commun. **5**, 3786 (2014).

[6] Z. Liu, J. Jiang, B. Zhou, Z. Wang, Y. Zhang, H. Weng, D. Prabhakaran, S. Mo, H. Peng, P. Dudin *et al.*, Nat. Mater. **13**, 677 (2014).

[7] S. Borisenko, Q. Gibson, D. Evtushinsky, V. Zabolotnyy, B. Büchner, and R. J. Cava, Phys. Rev. Lett. **113**, 027603 (2014).

[8] T. Liang, Q. Gibson, M. N. Ali, M. Liu, R. Cava, and N. Ong, Nat. Mater. **14**, 280 (2015).

[9] C.-Z. Li, L.-X. Wang, H. Liu, J. Wang, Z.-M. Liao, and D.-P. Yu, Nat. Commun. **6**, 10137 (2015).

[10] H. Li, H. He, H. Lu, H. Zhang, H. Liu, R. Ma, Z. Fan, S. Shen, and J. Wang, Nat. Commun. **7**, 10301 (2015).

[11] T. Wehling, A. M. Black-Schaffer, and A. V. Balatsky, Adv. Phys. **63**, 1 (2014).

[12] X. Wan, A. M. Turner, A. Vishwanath, and S. Y. Savrasov, Phys. Rev. B **83**, 205101 (2011).

[13] Z. Fang, N. Nagaosa, K. S. Takahashi, A. Asamitsu, R. Mathieu, T. Ogasawara, H. Yamada, M. Kawasaki, Y. Tokura, and K. Terakura, Science **302**, 92 (2003).

[14] H. Weng, C. Fang, Z. Fang, B. A. Bernevig, and X. Dai, Phys. Rev. X **5**, 011029 (2015).

[15] S.-Y. Xu, I. Belopolski, N. Alidoust, M. Neupane, G. Bian, C. Zhang, R. Sankar, G. Chang, Z. Yuan, C.-C. Lee *et al.*, Science **349**, 613 (2015).

[16] S.-M. Huang, S.-Y. Xu, I. Belopolski, C.-C. Lee, G. Chang, B. Wang, N. Alidoust, G. Bian, M. Neupane, C. Zhang *et al.*, Nat. Commun. **6**, 7373 (2015).

[17] B. Q. Lv, H. M. Weng, B. B. Fu, X. P. Wang, H. Miao, J. Ma, P. Richard, X. C. Huang, L. X. Zhao, G. F. Chen, Z. Fang, X. Dai, T. Qian, and H. Ding, Phys. Rev. X **5**, 031013 (2015).

[18] B. Q. Lv, N. Xu, H. M. Weng, J. Z. Ma, P. Richard, X. C. Huang, L. X. Zhao, G. F. Chen, C. E. Matt, F. Bisti *et al.*, Nat. Phys. **11**, 724 (2015).

[19] S.-Y. Xu, N. Alidoust, I. Belopolski, Z. Yuan, G. Bian, T.-R. Chang, H. Zheng, V. N. Strocov, D. S. Sanchez, G. Chang *et al.*, Nat. Phys. **11**, 748 (2015).

[20] S.-Y. Xu, I. Belopolski, D. S. Sanchez, C. Zhang, G. Chang, C. Guo, G. Bian, Z. Yuan, H. Lu, T.-R. Chang *et al.*, Sci. Adv. **1**, e1501092 (2015).

[21] N. Xu, H. Weng, B. Lv, C. Matt, J. Park, F. Bisti, V. Strocov, D. Gawryluk, E. Pomjakushina, K. Conder *et al.*, Nat. Commun. **7**, 11006 (2016).

[22] Z. Liu, L. Yang, Y. Sun, T. Zhang, H. Peng, H. Yang, C. Chen, Y. Zhang, Y. f. Guo, D. Prabhakaran *et al.*, Nat. Mater. **15**, 27 (2016).

[23] X. Huang, L. Zhao, Y. Long, P.Wang, D. Chen, Z. Yang, H. Liang, M. Xue, H. Weng, Z. Fang *et al.*, Phys. Rev. X **5**, 031023 (2015).

[24] C.-L. Zhang, S.-Y. Xu, I. Belopolski, Z. Yuan, Z. Lin, B. Tong, G. Bian, N. Alidoust, C.-C. Lee, S.-M. Huang *et al.*, Nat. Commun. **7**, 10735 (2016).

[25] F. Arnold, C. Shekhar, S.-C. Wu, Y. Sun, R. D. Dos Reis, N. Kumar, M. Naumann, M. O. Ajeesh, M. Schmidt, A. G. Grushin *et al.*, Nat. Commun. **7**, 11615 (2016).

[26] J. L. Manes, Phys. Rev. B **85**, 155118 (2012).

[27] B. Bradlyn, J. Cano, Z. Wang, M. Vergniory, C. Felser, R. J. Cava, and B. A. Bernevig, Science **353**, aaf5037 (2016).

[28] P. Tang, Q. Zhou, and S.-C. Zhang, Phys. Rev. Lett. **119**, 206402 (2017).

[29] W. Rarita and J. Schwinger, Phys. Rev. **60**, 61 (1941).

[30] L. Liang and Y. Yu, Phys. Rev. B **93**, 045113 (2016).

[31] M. Ezawa, Phys. Rev. B **94**, 195205 (2016).

[32] Y. Xu and L.-M. Duan, Phys. Rev. A **94**, 053619 (2016).

[33] T. Zhang, Z. Song, A. Alexandradinata, H. Weng, C. Fang, L. Lu, and Z. Fang, Phys. Rev. Lett. **120**, 016401 (2018).

[34] G. Chang, S.-Y. Xu, B. J. Wieder, D. S. Sanchez, S.-M. Huang, I. Belopolski, T.-R. Chang, S. Zhang, A. Bansil, H. Lin *et al.*, Phys. Rev. Lett. **119**, 206401 (2017).

[35] D. Pshenay-Severin, Y. V. Ivanov, A. Burkov, and A. Burkov, J. Phys: Condens. Matter **30**, 135501 (2018).

[36] D. S. Sanchez, I. Belopolski, T. A. Cochran, X. Xu, J.-X. Yin, G. Chang, W. Xie, K. Manna, V. Süß, C.-Y. Huang *et al.*, Nature (London) **567**, 500 (2019).

[37] D. Takane, Z. Wang, S. Souma, K. Nakayama, T. Nakamura, H. Oinuma, Y. Nakata, H. Iwasawa, C. Cacho, T. Kim *et al.*, Phys. Rev. Lett. **122**, 076402 (2019).

[38] Z. Rao, H. Li, T. Zhang, S. Tian, C. Li, B. Fu, C. Tang, L. Wang, Z. Li, W. Fan *et al.*, Nature (London) **567**, 496 (2019).

[39] X. Xu, X. Wang, T. A. Cochran, D. S. Sanchez, G. Chang, I. Belopolski, G. Wang, Y. Liu, H.-J. Tien, X. Gui *et al.*, Phys. Rev. B **100**, 045104 (2019).

[40] D. Wu, Z. Mi, Y. Li, W. Wu, P. Li, Y. Song, G. Liu, G. Li, and J. Luo, Chin. Phys. L **36**, 077102 (2019).

[41] N. B. Schröter, D. Pei, M. G. Vergniory, Y. Sun, K. Manna, F. De Juan, J. A. Krieger, V. Süss, M. Schmidt, P. Dudin *et al.*, Nat. Phys. **15**, 759 (2019).

[42] M. Yao, K. Manna, Q. Yang, A. Fedorov, V. Voroshnin, B. V. Schwarze, J. Hornung, S. Chattopadhyay, Z. Sun, S. N. Guin *et al.*, Nat. Commun. **11**, 2033 (2020).

[43] S. Xu, L. Zhou, X.-Y. Wang, H. Wang, J.-F. Iin, X.-Y. Zeng, P. Cheng, H. Weng, T.-L. Xia *et al.*, arXiv:2003.13397.

[44] H. Li, S. Xu, Z.-C. Rao, L.-Q. Zhou, Z.-J. Wang, S.-M. Zhou, S.-J. Tian, S.-Y. Gao, J.-J. Li, Y.-B. Huang *et al.*, Nat. Commun. **10**, 1 (2019).

[45] S. Xu, L. Zhou, H. Wang, X.-Y. Wang, Y. Su, P. Cheng, H. Weng, and T.-L. Xia, Phys. Rev. B **100**, 245146 (2019).

[46] N. Schröter, S. Stolz, K. Manna, F. de Juan, M. G. Vergniory, J. A. Krieger, D. Pei, T. Schmitt, P. Dudin, T. K. Kim, C. Cacho *et al.*, Science **369**, 179 (2020).

[47] P. E. Blöchl, Phys. Rev. B **50**, 17953 (1994).

[48] G. Kresse and D. Joubert, Phys. Rev. B **59**, 1758 (1999).

[49] G. Kresse and J. Hafner, Phys. Rev. B **47**, 558 (1993).

[50] G. Kresse and J. Furthmüller, Comput. Mater. Sci. **6**, 15 (1996).

[51] G. Kresse and J. Furthmüller, Phys. Rev. B **54**, 11169 (1996).

[52] J. P. Perdew, K. Burke, and M. Ernzerhof, Phys. Rev. Lett. **78**, 1396 (1997).

[53] L. Pauling and A. Soldate, Acta Crystallogr. **1**, 212 (1948).

[54] N. Marzari and D. Vanderbilt, Phys. Rev. B **56**, 12847 (1997).

[55] I. Souza, N. Marzari, and D. Vanderbilt, Phys. Rev. B **65**, 035109 (2001).

[56] D. Shoenberg, *Magnetic Oscillations in Metals* (Cambridge University Press, Cambridge, UK, 2009).

[57] See Supplemental Material at http://link.aps.org/supplemental/ 10.1103/PhysRevB.102.115129 for the multiple peak analysis and fits of FFT spectra, the Berry phase of hole pocket at Γ point and additional detailed profile of electron pockets.

[58] A. Kokalj, Comput. Mater. Sci. **28**, 155 (2003).